Perpendicular Magnetic Anisotropy and High Spin Polarization in Tetragonal $Fe_4N/BiFeO_3$ Heterostructures

Li Yin,[1] Wenbo Mi,[1,*] and Xiaocha Wang[2]

[1]*Tianjin Key Laboratory of Low Dimensional Materials Physics and Preparation Technology & Key Laboratory of Advanced Ceramics and Machining Technology of Ministry of Education, Faculty of Science, Tianjin University, Tianjin 300354, China*

[2]*School of Electronics Information Engineering, Tianjin University of Technology, Tianjin 300384, China*

(Received 4 August 2016; revised manuscript received 17 October 2016; published 29 December 2016)

The tetragonal $Fe_4N/BiFeO_3(001)$ heterostructures aimed at simultaneously gaining the perpendicular magnetic anisotropy (PMA) and high spin polarization have been investigated by the first-principles method. It is found that Fe_4N with Fe_AFe_B termination is better for achieving interfacial and inner PMA simultaneously than $(Fe_B)_2N$ termination. When the positions of interfacial Fe_A and Fe_B relative to Fe in $BiFeO_3$ are changed, the PMA in Fe_4N transforms into the in-plane magnetic anisotropy. Especially, PMA in Fe_4N near the heterointerfaces depends on the direction of ferroelectric polarization in $BiFeO_3$. Finally, the interfacial and inner PMA of Fe_4N along with high spin polarization appear in the stable $Fe_AFe_B/Fe\text{-}O_2$ case owing to the $3d$-$3d$ orbital hybridization. These results provide the opportunities for developing multifunctional spintronic devices.

DOI: 10.1103/PhysRevApplied.6.064022

I. INTRODUCTION

Perpendicular magnetic anisotropy (PMA) has attracted much attention because of its potential applications in magnetic random access memories (MRAM) [1,2]. Ferromagnetic PMA electrodes demand a smaller critical current to switch the magnetization in a spin-transfer-torque MRAM (STT MRAM) [3], which is very important in energy-efficient devices. So far, PMA appears in distinct systems, such as the interfaces between magnetic Co and heavy nonmagnetic transition metals due to $3d$-$5d$ orbital hybridizations [4] and the individual Os adatom on the MgO surface in the stable adsorption sites [5], etc. PMA in the magnetic tunnel junctions (MTJs) are investigated in the experiments and theoretical calculations [3,6]. However, most of the ferromagnets with PMA have relatively low spin polarization, while the high spin-polarized electrodes are necessary for the multifunctional spintronic devices. Therefore, exploring PMA in the highly spin-polarized ferromagnets can establish the foundations for the high-performance spintronic devices.

Ferromagnetic Fe_4N with a cubic perovskite-type lattice [7,8] has a high Curie temperature of 760 K, a large spin polarization of nearly 100% [9], and excellent chemical stability. Fe_4N is a soft ferromagnet with a large saturation magnetization and a low coercivity. All of these characteristics benefit MTJs, where a large tunnel magnetoresistance is achieved in Fe_4N-based MTJs [10]. PMA in Fe_4N is meaningful to the related magnetic devices, especially the energy-efficient STT MRAM [3]. Recently, the tetragonal distortion has been demonstrated to induce the PMA in the cubic ferromagnets because the magnetization can be aligned at the tetragonal axis [11]. So, we attempt to produce the tetragonal distortion in Fe_4N by forming the heterostructures, which is an effective approach to induce PMA in various materials [4,6,12]. The interplay of charge, spin, lattice, and orbital degrees of freedom at the heterointerfaces provides a solid ground for PMA [13]. Moreover, magnetic anisotropy (MA) in the heterostructures can be modulated by the intrinsic interfacial conditions [14,15], current and electric field [16,17].

Different from the common heavy metals and MgO [3–6], we choose $BiFeO_3$ (BFO) as a substrate to introduce the tetragonal distortion in Fe_4N, which is the only known room-temperature single-phase multiferroic phase with a G-type antiferromagnetic order [18]. Experimentally, the lattice constants of tetragonal BFO are $a = 3.770$ Å and $c/a = 1.233$ [19,20], which has a small ab-lattice mismatch of 0.7% with cubic Fe_4N ($a = 3.795$ Å) [21]. Tetragonal BFO in space group $P4mm$ has a large spontaneous ferroelectric polarization of 150 $\mu C/cm^2$ [19,22], a large charge transfer excitation [23], and a large resistance change in the ferroelectric tunnel junctions [20]. If the tetragonal BFO could induce a high PMA in the spin-polarized Fe_4N, the large ferroelectric polarization in BFO can further modulate the high spin-polarized PMA [20,24], which will expand the practical applications in the multifunctional spintronic devices and the physical prospects of the high spin-polarized PMA [18]. In this paper, we investigate the PMA and spin polarization of the tetragonal $Fe_4N/BFO(001)$ heterostructures with different terminations,

*Author to whom all correspondence should be addressed. miwenbo@tju.edu.cn

interfacial atomic positions, and ferroelectric polarization. It is found that the interfacial and inner PMA in Fe_4N along with a high spin polarization appears in the Fe_AFe_B/Fe-O_2 model thanks to the $3d$-$3d$ orbital hybridization.

II. CALCULATION DETAILS AND MODELS

The calculations are performed in the Vienna *ab initio* simulation package based on the projector augment-wave pseudopotentials and Perdew-Burke-Ernzerhof flavor of the spin-polarized generalized gradient approximation [25,26]. The convergence criteria for the energy and atomic forces are set to 10^{-5} eV and 0.02 eV/Å, respectively. The energy cutoff for the plane-wave basis set is 500 eV. In the z direction, a 15-Å vacuum space is used to separate the interaction between periodic images in the tetragonal Fe_4N/BFO heterostructures. The Brillouin zone is sampled with Γ-centered $5\times5\times5$, $9\times9\times9$, and $5\times5\times1$ k-point meshes for bulk BFO($2\times2\times2$), $Fe_4N(1\times1\times1)$, and Fe_4N/BFO($\sqrt{2}\times\sqrt{2}$) supercells, respectively. Additionally, the tested on-site Coulomb repulsion of $U=4.5(0.0)$ eV is included for Fe $3d$ states in BFO(Fe_4N) [27]. Four Fe_4N/BFO models including 7-layered Fe_4N and 7-layered BFO along the [001] direction are built with a $p(\sqrt{2}\times\sqrt{2})$ periodicity (Fig. 1). The fabrication methods of epitaxial heterostructures, such as the pulsed laser deposition and molecular beam epitaxy [28–30], have been improved significantly and have reached atomic-scale precision. Meanwhile, the epitaxial tetragonal BFO and Fe_4N films have been experimentally fabricated [20,29,31], so the tetragonal Fe_4N/BFO with a small lattice mismatch may be realized in the experiments. Therefore, by assuming that Fe_4N grows on the tetragonal BFO, we fix the xy-plane lattice constants of the tetragonal Fe_4N/BFO heterostructures at BFO's values. Atoms at the bottom three layers of BFO are fixed at its bulk position, and other atoms are fully relaxed.

The cohesive energy is defined as $W_{\rm coh}=E_{\rm Fe_4N}+E_{\rm BFO}-E_{\rm Fe_4N/BFO}$, where $E_{\rm Fe_4N/BFO}$ is the total energy of heterostructures, and $E_{\rm Fe_4N}$ and $E_{\rm BFO}$ represent the energy of the same supercells containing either Fe_4N or BFO parts. A larger $W_{\rm coh}$ suggests a more stable structure. The charge-density difference is also calculated by subtracting the charge densities of the isolated BFO and Fe_4N from the heterostructures. Magnetic anisotropy energy (MAE) is calculated by considering the spin-orbit coupling (SOC) [1,2]. In order to label the PMA and in-plane MA (IMA), the total MAE is decomposed over different orbital λ of atom i with the so-called canonical formulation [1,2]

$$\mathrm{MAE}_{i\lambda}=\left[\int^{E_F^{\rm out}}(E-E_F^{\rm in})n_{i\lambda}^{\rm out}(E)dE-\int^{E_F^{\rm in}}(E-E_F^{\rm in})n_{i\lambda}^{\rm in}(E)dE\right]/a^2, \quad (1)$$

where $n_{i\lambda}^{\rm out}(E)$ and $n_{i\lambda}^{\rm in}(E)$ are the density of states on the orbital λ of atom i in the out-of-plane and in-plane magnetization orientations, and a is the in-plane lattice constant. The MAE of atom i is obtained with λ for all of the orbitals [2]

$$\mathrm{MAE}_i=\sum_\lambda \mathrm{MAE}_{i\lambda}, \quad (2)$$

then the sum of MAE_i over all of the atoms gives the total MAE [2]. Based on the layer- and orbital-resolved MAE method, we analyze the MAE layer distribution of Fe_4N in different Fe_4N/BFO models. Besides, the spatial spin polarization (SSP) is defined as

$$P(r,z,\varepsilon)=\frac{n_s^{\uparrow}(r,z,\varepsilon)-n_s^{\downarrow}(r,z,\varepsilon)}{n_s^{\uparrow}(r,z,\varepsilon)+n_s^{\downarrow}(r,z,\varepsilon)}, \quad (3)$$

where the $n_s^{\uparrow(\downarrow)}(r,z,\varepsilon)$ is the spin-up (spin-down) charge density in real space with an energy interval of $[\varepsilon, E_F]$, at position r and a distance z from the layer VII in Fe_4N [32].

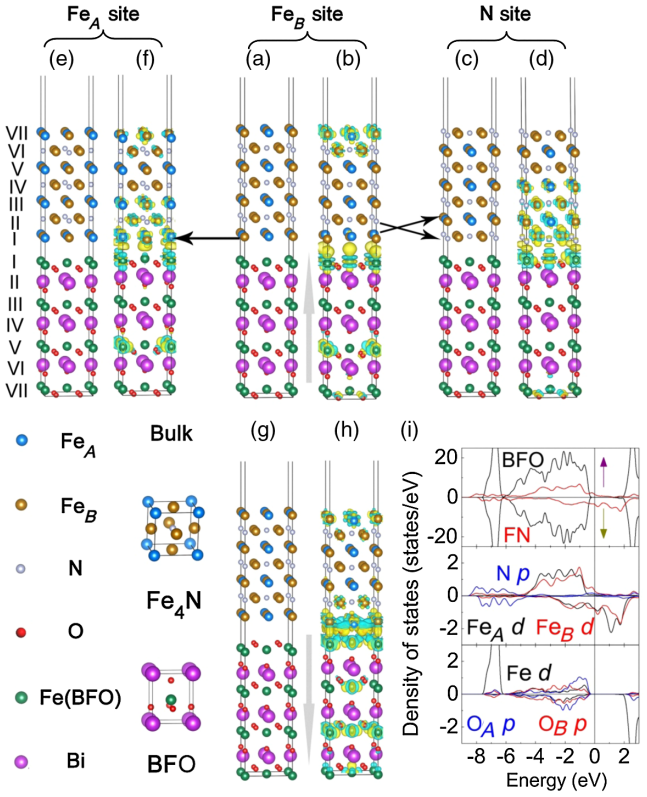

FIG. 1. Structures and charge-density difference of Fe_4N/BFO heterostructures for (a),(b) Fe_AFe_B/Fe-O_2, (c),(d) $(Fe_B)_2N$/Fe-O_2, (e),(f) Fe_BFe_A/Fe-O_2, (g),(h) Fe_AFe_B/O_2-Fe models (isosurface value 0.006 e/Å^3). Side views of bulk Fe_4N and BFO. Fe_A, Fe_B, and N of bulk Fe_4N are located in the corner, face-centered, and body-centered sites, respectively. The Fe_A site (Fe_B site, N site) indicates that Fe_A (Fe_B, N) atoms in the Fe_4N-I layer are at the top of Fe in the BFO-I layer. The gray arrows indicate the polarized direction of BFO. The yellow (blue) isosurfaces represent the charge accumulation (depletion). (i) Total and partial DOS for bulk Fe_4N and BFO. $E_F=0$ eV.

III. RESULTS AND DISCUSSION

First, the characteristics of bulk BFO and Fe_4N are analyzed in detail. The relaxed BFO has $c/a = 1.233$, which is identical with the experimental results [20]. The z-directional Bi-O_A (Fe-O_B) planar displacement of 0.792 (0.673) Å is consistent with previously calculated results, where O_A and O_B in the O octahedron locate at the FeO_2 plane and apical site, respectively [19]. In Fig. 1(i), the total and partial DOS of BFO are similar to previously calculated results [27]. The calculated band gap of 1.93 eV is consistent with previously calculated 1.90 eV [27]. The Fe magnetic moments of $\pm 4.18\mu_B$ are in good agreement with experimental $4.34\mu_B$ and calculated $4.18\mu_B$ [27,33]. Herewith, the atoms and z-directional lattice constant of Fe_4N are fully relaxed, but the xy-plane lattice constants are fixed at BFO's values. In Fig. 1(i), the total DOS of the ab-fixed Fe_4N at E_F still mainly comes from the spin-down channel. The strong hybridization between N p and Fe_B d states in the energy range from -8.5 to -5.0 eV results in a smaller Fe_B moment of 2.31 μ_B than Fe_A of 2.95 μ_B, see Fig. 1(i), which is similar to the fully relaxed Fe_4N [21]. These results demonstrate that the calculations are reliable. Next, we will focus on the tetragonal Fe_4N/BFO heterostructures.

Since Bi^{3+} is volatile as BFO grows in experiments, the FeO_2 termination of BFO is considered in all of the tetragonal Fe_4N/BFO models. In Fig. 1(a), the probably stable Fe_AFe_B/Fe-O_2 model is set up, where the Fe_A(Fe_B) positions in the interfacial I layer are analogous with Bi(O) cases due to their similar corner (face-centered) sites in bulks. Then, in Figs. 1(e) and 1(e), we further build the $(Fe_B)_2N$/Fe-O_2 model with specific $(Fe_B)_2N$ terminations and the Fe_BFe_A/Fe-O_2 model with different interfacial atomic positions. Furthermore, we change the direction of ferroelectric polarization of BFO in the tetragonal Fe_4N/BFO heterostructures, as shown in Figs. 1(g) and 1(g).

In Table I, the calculated cohesive energy indicates that the Fe_AFe_B/Fe-O_2 and Fe_AFe_B/O_2-Fe models are more stable than the other two cases. The label "FN-I-Fe_A" refers to Fe_A in layer I which locates in Fe_4N. Meanwhile, the same definitions will be used in the whole text. Although the atoms in both FN-I and FN-VII layers exhibit apparent z-directional polar displacements, see the insets of Fig. 2(e), the interfacial FN-I layer exhibits more obvious displacements than the surface FN-VII of each model. In Fig. 1, an apparent charge accumulation exists between BFO-I-Fe and its apical (Fe_A, Fe_B, or N) atoms in the related models. The above results reveal a strong but various interfacial effect in four Fe_4N/BFO models.

In Fig. 3(a), Fe_4N in the Fe_AFe_B/Fe-O_2 model shows PMA in all the seven layers, where the maximum PMA is -5 erg/cm^2. The maximum PMA is stronger than Fe of 3 erg/cm^2 in the Fe/MgO interfaces [6]. However, in Fig. 3(b), Fe_4N in the $(Fe_B)_2N$/Fe-O_2 case only shows PMA in the FN-I and FN-II layers. In Figs. 2(e) and 2(e), the evident FN-I displacements and charge accumulations between BFO-I-Fe and FN-I-N demonstrate that the strong interfacial coupling exists in the $(Fe_B)_2N$/Fe-O_2 model. The

TABLE I. The calculated spin magnetic moment of interfacial atoms without and with SOC for each model. The double values for Fe_A(Fe_B) moments in one position are due to the antiferromagnetic properties of BFO. Differences of spin magnetic moments along [100] and [001] are less than 0.001 μ_B for each atom. The values of $z1$–$z3$ (see Fig. 2) indicate the distances of I–III, III–V, and V–VII layers in Fe_4N along [001]. W_{coh} is the cohesive energy.

	Model	Bulk	Fe_AFe_B/Fe-O_2	$(Fe_B)_2N$/Fe-O_2	Fe_BFe_A/Fe-O_2	Fe_AFe_B/O_2-Fe
Moments (μ_B)	BFO-I-Fe	± 4.177	3.827/ − 3.799	4.098/ − 3.460	3.950/ − 3.939	3.652/ − 3.650
	BFO-II-O_A	± 0.218	−0.188/0.192	−0.178/0.211	−0.174/0.182	0.077/ − 0.035
	FN-I-Fe_A	2.950	2.912/2.911	⋯	−0.155/1.078	3.294/3.307
	FN-I-Fe_B	2.329	2.493/2.610	0.431/0.398	2.950/2.909	−2.582/ − 2.778
	FN-I-N	⋯	⋯	−0.016/ − 0.006	⋯	⋯
	FN-II-Fe_A	⋯	⋯	−2.882/ − 2.889	⋯	⋯
	FN-II-Fe_B	2.281	2.008/1.940	0.785/1.096	−1.950/ − 2.031	2.250/2.209
	FN-II-N	0.022	−0.015/0.019	⋯	0.028/0.029	0.000/ − 0.003
Moments (μ_B) including SOC	BFO-I-Fe	⋯	3.832/ − 3.803	4.092/ − 4.051	3.933/ − 3.885	3.710/ − 3.650
	BFO-II-O_A	⋯	−0.175/0.180	−0.186/0.187	−0.185/0.196	0.096/ − 0.063
	FN-I-Fe_A	⋯	2.912/2.912	⋯	−1.103/ − 0.388	3.415/3.415
	FN-I-Fe_B	⋯	2.496/2.610	0.072/0.072	2.853/2.853	−2.654/2.817
	FN-I-N	⋯	⋯	0.029/ − 0.032	⋯	⋯
	FN-II-Fe_A	⋯	⋯	−0.338/ − 0.338	⋯	⋯
	FN-I-Fe_B	⋯	1.979/1.979	1.727/ − 1.452	1.835/1.834	−2.087/ − 2.087
	FN-II-N	⋯	−0.012/0.021	⋯	−0.001/ − 0.001	0.020/0.031
	$z1$ (Å)		3.802	3.919	3.831	4.205
	$z2$ (Å)		3.827	3.770	3.800	3.725
	$z3$ (Å)		3.817	3.828	3.810	3.510
	W_{coh} (eV)	⋯	3.929	−1.721	0.802	7.381

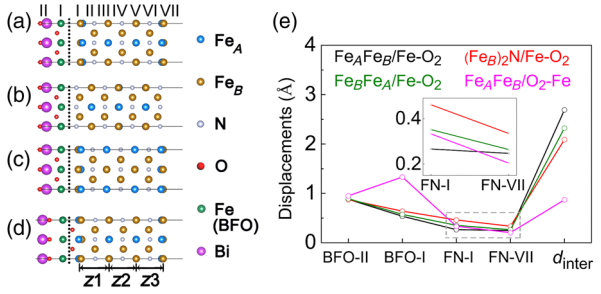

FIG. 2. Relaxed geometries of (a) Fe_AFe_B/Fe-O_2, (b) $(Fe_B)_2$N/Fe-O_2, (c) Fe_BFe_A/Fe-O_2, and (d) Fe_AFe_B/O_2-Fe models. (e) The z-directional Fe(Bi)-O and Fe_B-Fe_A(N) polar displacements in one layer. Distances between BFO-I and FN-I heterointerfaces (d_{inter}) are displayed.

strong interfacial coupling makes its $z1$ distance much larger than $z2$, $z3$, and a(3.770 Å), as shown in Fig. 2(b) and Table I. We suggest that the prominent tetragonal distortion from FN-I to FN-III layers probably favors to the layer-resolved PMA of FN-I and FN-II in the $(Fe_B)_2$N/Fe-O_2 case. However, the tetragonal distortion cannot totally determine MA because the interfacial couplings also have a dramatic influence on MA. So, the Fe_AFe_B termination is better for obtaining the interfacial and inner PMA than $(Fe_B)_2$N. Therefore, we will further change the interfacial conditions in the Fe_AFe_B-terminated models.

In Figs. 1(e) and 1(e), the Fe_BFe_A/Fe-O_2 and Fe_AFe_B/Fe-O_2 models have the same termination, but the positions of FN-I-Fe_A and FN-I-Fe_B are changed with respect to BFO-I-Fe. In Fig. 3(c), Fe_4N in the Fe_BFe_A/Fe-O_2 model shows IMA, which is the opposite of the PMA in the Fe_AFe_B/Fe-O_2 case because of the different interfacial exchange couplings. Herewith, the orbitals such as d_{xy} and d_{z^2} are defined by considering the unit cell sides of the heterostructures. In the FN-I layer of Fig. 4(a), the highest

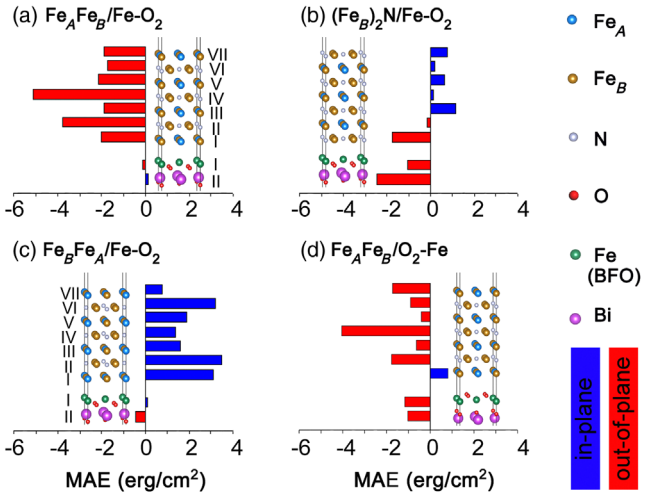

FIG. 3. Layer-resolved MAE of each model with GGA + U + SOC calculations.

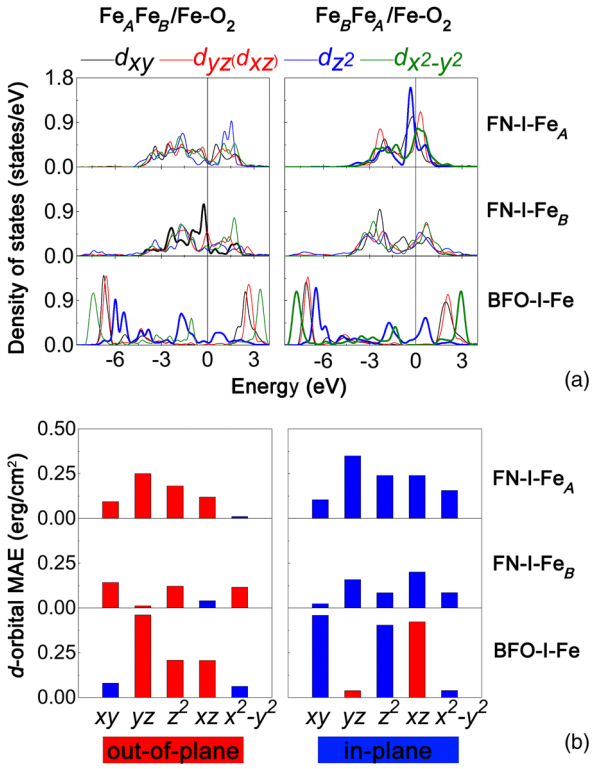

FIG. 4. (a) DOS of Fe atoms and (b) its orbital-resolved MAE at FeAFeB/Fe-O2 (left panel) and Fe_BFe_A/Fe-O_2 (right panel) heterointerfaces with GGA + U + SOC calculations.

peak of partial DOS comes from FN-I-Fe_B in the Fe_AFe_B/Fe-O_2 model and FN-I-Fe_A in the Fe_BFe_A/Fe-O_2 case, respectively. However, the highest peak is located at −0.23 eV for both Fe_AFe_B/Fe-O_2 and Fe_BFe_A/Fe-O_2 cases. Especially, BFO-I-Fe d_{z^2} and FN-I-Fe_B d_{xy} show an obvious hybridization at −0.23 eV in the Fe_AFe_B/Fe-O_2 model, but in Fig. 4(a), the hybridization disappears in the Fe_BFe_A/Fe-O_2 case. On the contrary, in the right panel of Fig. 4(a), d_{z^2} ($d_{x^2-y^2}$) states of BFO-I-Fe and FN-I-Fe_A strongly hybridize in the energy range from −2.05 to −0.75 eV in the Fe_BFe_A/Fe-O_2 model. Meanwhile, in Figs. 1(f) and 1(f), a large charge accumulation appears at the interfacial Fe_B site and Fe_A site in the two models, respectively. So, the Fe_BFe_A/Fe-O_2 interfaces show a stronger interaction between BFO-I-Fe and FN-I-Fe_A, which makes it a different MA from the Fe_AFe_B/Fe-O_2 model, although the two models contain almost the identical distortions in Fig. 2. Furthermore, in Table I, the two models contain almost the same $z3$, which is the z-directional distance between the FN-V and FN-VII layers. Therefore, the same atomic component and similar tetragonal distortion from FN-V to FN-VII layers exists in the two models. All of these results indicate that different MAE between the Fe_BFe_A/Fe-O_2 and Fe_AFe_B/Fe-O_2 models can mainly be ascribed to the distinct interfacial exchange interactions near the FN-I layer, rather than the surface effect near the FN-VII layer [34].

The orbital-resolved MAE of Fe_BFe_A/Fe-O_2 and Fe_AFe_B/Fe-O_2 models are totally distinct. In Fig. 4(a), BFO-I-Fe d_{z^2} hybridizes with FN-I-Fe_A d_{yz} (d_{xz}) and FN-I-Fe_B d_{xy} at −0.23 eV in the Fe_AFe_B/Fe-O_2 model. In Fig. 4(b), the hybridized d_{yz} and d_{xy} are the main contribution of d-resolved MAE in FN-I-Fe_A and FN-I-Fe_B, respectively. In the Fe_BFe_A/Fe-O_2 model, FN-I-Fe_A $d_{x^2-y^2}$ states that hybridize with BFO-I-Fe make a larger contribution to the d-resolved MAE than FN-I-Fe_A in the Fe_AFe_B/Fe-O_2 case [Fig. 4(b)]. These results suggest that the interfacial $3d$-$3d$ hybridization between BFO-I-Fe and FN-I-Fe_B(Fe_A) are essentially associated with the PMA of Fe_AFe_B/Fe-O_2 and IMA of Fe_BFe_A/Fe-O_2. In Fig. 4(a), although the partial DOS of d_{yz} and d_{xz} overlap, the two orbitals are not completely equivalent and their contributions to MAE are different [Fig. 4(b)], which may be associated with the massive charge reconstructions owing to the interfacial coupling [Figs. 1(f) and 1(f)]. Meanwhile, in Fig. 4(b), MAE differences of d_{yz} and d_{xz} in the Fe_AFe_B/Fe-O_2 model are distinct from the Fe_BFe_A/Fe-O_2 case, which is owing to their distinct interfacial couplings. In Table I, another important point is that the magnetic moments of the $(Fe_B)_2N$/Fe-O_2 and Fe_BFe_A/Fe-O_2 models decrease remarkably, where the ferromagnetic order of Fe_4N is destroyed. However, the ferromagnetic order of Fe_4N is maintained in the stable Fe_AFe_B/Fe-O_2 case, where the whole Fe_4N region exhibits PMA, which is significant to spintronic devices.

In order to utilize the ferroelectric character of tetragonal BFO, we change the direction of ferroelectric polarization of tetragonal BFO in the Fe_AFe_B/Fe-O_2 case [Fig. 1(a)] and the opposite-polarized direction in the Fe_AFe_B/O_2-Fe model [Fig. 1(g)] is built. In Figs. 3(d) and 3(d), the interfacial FN-I layer transforms from PMA in the Fe_AFe_B/Fe-O_2 model into IMA in the Fe_AFe_B/O_2-Fe model. According to MAE and magnetic moments of each atom, in Figs. 5(b) and 5(b), we draw the diagrams of Fe_4N's magnetic order in the Fe_AFe_B/Fe-O_2 and Fe_AFe_B/O_2-Fe models, respectively. The ferromagnetic order of Fe_4N is clearly damaged in the Fe_AFe_B/O_2-Fe model and Fe_A tends to be an antiferromagnetic order [Fig. 5(b)]. However, the weak PMA and broken ferromagnetic order of Fe_4N in the Fe_AFe_B/O_2-Fe case is very different from the high PMA and ferromagnetic order in the Fe_AFe_B/Fe-O_2 case. The large difference reveals that the Fe_AFe_B/BFO-based MTJs might exhibit the controllable high and low magnetoresistance by changing the direction of ferroelectric polarization in BFO [3,10]. Besides, in Table I, the tetragonal distortion of the Fe_AFe_B/O_2-Fe model is more prominent than the $(Fe_B)_2N$/Fe-O_2 model. However, in Fig. 3(d), the FN-I layer in the Fe_AFe_B/O_2-Fe model still shows the in-plane MA owing to the specific interfacial exchange interaction. In four heterostructures, the smallest interfacial distance appears in the Fe_AFe_B/O_2-Fe model [Fig. 2(e)], which is tightly related to the strong charge accumulation of BFO-I-O [Fig. 1(h)]. The high activity of BFO-I-O atoms may be the nominal oxidation states of Fe atoms [7,8].

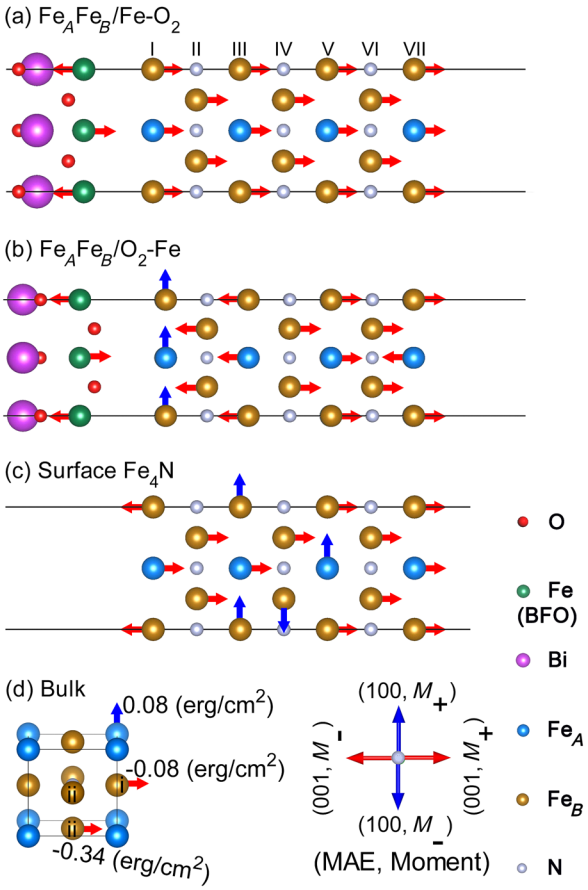

FIG. 5. The magnetic order of (a) Fe_AFe_B/Fe-O_2, (b) Fe_AFe_B/O_2-Fe, (c) slab, and (d) bulk Fe_4N, based on the MAE and magnetic moment with GGA + U + SOC calculations. The slab Fe_4N is extracted from the Fe_AFe_B/Fe-O_2 model. Fe_B in Fe_AFe_B(001) and $(Fe_B)_2N$(001) planes are defined as Fe_B(i) and Fe_B(ii), respectively. M_+ (M_-) indicates the magnetic moment with positive (negative) values.

Aimed at analyzing the magnetization of Fe_4N before and after attaching BFO, we further calculate the moment direction of bulk and slab Fe_4N. Three nonequivalent Fe ions of Fe_A, Fe_B(i), and Fe_B(ii) appear in the ab-fixed bulk Fe_4N, which is consistent with previous results [7,8]. The magnetic moment of Fe_A, Fe_B(i), and Fe_B(ii) in bulk Fe_4N is 2.95, 2.33, and 2.28μ_B, respectively. In Fig. 5(d), Fe_A exhibits IMA, Fe_B(i) shows weak PMA and Fe_B(ii) presents a strong PMA along the [001] direction. Particularly, in Fig. 5(d), the MAE of Fe_A and Fe_B(i) in bulk Fe_4N is apparently disadvantaged, as compared with FN-I-Fe_A and FN-I-Fe_B in the Fe_AFe_B/Fe-O_2 model [Fig. 4(b)]. In the slab of Fe_4N, both IMA and PMA exist and the ferromagnetic order is broken in layer I. However, in Fig. 5(a), Fe_4N in the Fe_AFe_B/Fe-O_2 model shows PMA and the ferromagnetic order in the whole region. The distinct PMA of Fe_4N in bulk, slab, and Fe_AFe_B/Fe-O_2 structures demonstrates the BFO's

great influence on the magnetic characteristics of Fe_4N and reflects the advantage of Fe_4N/BFO heterostructures.

Our intention is to realize PMA and high spin polarization simultaneously, so we will distinguish the spin-up and spin-down DOS under the GGA + U + SOC calculations and study the spin polarization of the advantaged Fe_AFe_B/Fe-O_2 case. Figure 6(a) shows the spin-distinguished DOS calculated by GGA + U + SOC, which is reliable and consistent with GGA + U. In Fig. 6(a), FN-I-Fe_A (Fe_B) has a spin polarization of nearly 100% (85%), and other atomic spin polarization (ASP) in Fe_4N are high. According to GGA + U calculation, we further investigate the spatial distribution of spin polarization in the energy intervals of $[E_F - 0.4\ \text{eV}, E_F]$ and $[E_F, E_F + 0.4\ \text{eV}]$. Considering the Fermi level can be tuned by many means, such as doping the substrate or applying a gate voltage [35], the spin polarization in the two energy intervals are analyzed. In Fig. 6(b), the SSP results indicate that the high spin polarization is widely distributed in the FN-I layer and BFO-I-Fe, which is in good agreement with the above ASP results. Moreover, in Fig. 6(c), the whole Fe_4N part in the Fe_AFe_B/Fe-O_2 model shows a high SSP. Our results indicate that the high spin polarization and PMA simultaneously appear in the Fe_AFe_B/Fe-O_2 model, which will provide an efficient spin-polarized current and improve the performances of spintronic devices, such as STT MRAM.

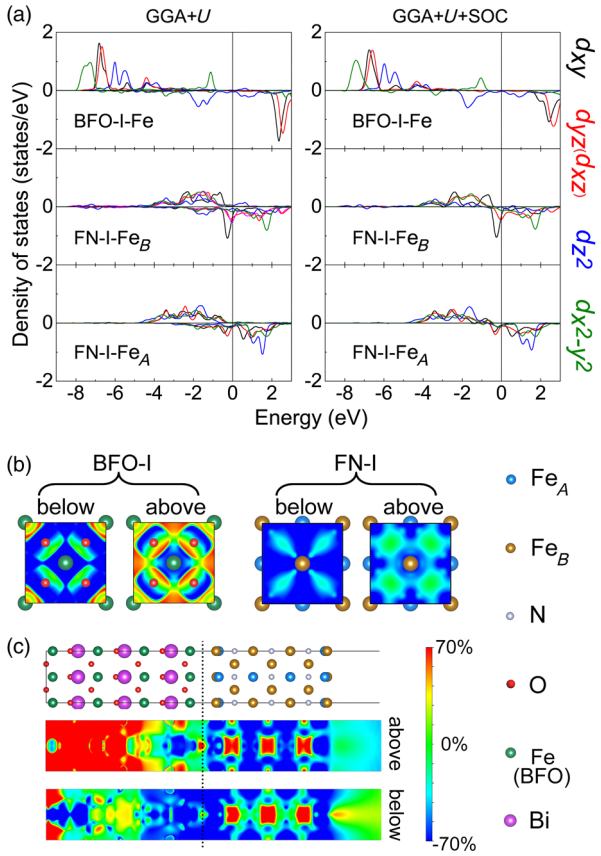

FIG. 6. (a) DOS of Fe atoms in the Fe_AFe_B/Fe-O_2 interface with GGA + U and GGA + U + SOC calculations, where positive (negative) values in the vertical axis represent spin-up and spin-down states. $E_F = 0$ eV. SSP of the BFO-I and FN-I layer in the (001) plane are shown in (b), and SSP in the (100) plane with a location of $0.5a$ are depicted in (c), under GGA + U calculation. The energy intervals of $[E_F - 0.4\ \text{eV}, E_F]$ and $[E_F, E_F + 0.4\ \text{eV}]$ match with the below and above labels of (b) and (c), respectively. The relaxed Fe_AFe_B/Fe-O_2 model is displayed in (c).

IV. CONCLUSION

In summary, we study the PMA and spin polarization of the tetragonal Fe_4N/BFO(001) heterostructures by the first-principles method. The main conclusions can be summarized as follows: (i) Fe_4N exhibits PMA in all the Fe_4N atomic layers of the Fe_AFe_B/Fe-O_2 model, but shows PMA only in the FN-I and FN-II layers of the $(Fe_B)_2N$/Fe-O_2 case, revealing that the Fe_AFe_B termination is better for achieving the interfacial and inner PMA than $(Fe_B)_2N$. (ii) As the position of interfacial Fe_A and Fe_B relative to BFO-Fe changes, PMA of Fe4N in the Fe_AFe_B/Fe-O_2 case transforms to IMA in the Fe_BFe_A/Fe-O_2 case. (iii) MA of the FN-I layer highly depends on the polarized direction of BFO. (iv) The interfacial and inner PMA of Fe_4N along with high spin polarization appears in the stable Fe_AFe_B/Fe-O_2 case owing to the interfacial $3d$-$3d$ orbital hybridization. It is found that the termination, interfacial atomic position, and ferroelectric polarization of BFO play an important role on PMA of the tetragonal Fe_4N/BFO heterostructures. The above results lay the foundations for developing the novel multifunctional spintronic devices. So, we hope that the theoretical prediction on PMA and high spin polarization can stimulate further experimental research.

ACKNOWLEDGMENTS

This work is supported by the National Natural Science Foundation of China (No. 51671142 and No. U1632152), the Key Project of Natural Science Foundation of Tianjin City (16JCZDJC37300), and the Program for New Century Excellent Talents in University (NCET-13-0409). It is also supported by the High Performance Computing Center of Tianjin University, China.

[1] A. Hallal, H. Yang, B. Dieny, and M. Chshiev, Anatomy of perpendicular magnetic anisotropy in Fe/MgO magnetic tunnel junctions: First-principles insight, Phys. Rev. B **88**, 184423 (2013).

[2] D. Li, C. Barreteau, M. Castell, F. Silly, and A. Smogunov, Out- versus in-plane magnetic anisotropy of free Fe and Co nanocrystals: tight-binding and first-principles studies, Phys. Rev. B **90**, 205409 (2014).

[3] S. Ikeda, K. Miura, H. Yamamoto, K. Mizunuma, H. Gan, M. Endo, S. Kanai, J. Hayakawa, F. Matsukura, and

H. Ohno, A perpendicular-anisotropy CoFeB-MgO magnetic tunnel junction, Nat. Mater. **9**, 721 (2010).
[4] D. Weller, Y. Wu, J. Stohr, M. Samant, B. Hermsmeier, and C. Chappert, Orbital magnetic moments of Co in multilayers with perpendicular magnetic anisotropy, Phys. Rev. B **49**, 12888 (1994).
[5] X. Ou, H. Wang, F. Fan, Z. Li, and H. Wu, Giant Magnetic Anisotropy of Co, Ru, and Os Adatoms on MgO (001) Surface, Phys. Rev. Lett. **115**, 257201 (2015).
[6] H. Yang, M. Chshiev, and B. Dieny, First-principles investigation of the very large perpendicular magnetic anisotropy at Fe/MgO and Co/MgO interfaces, Phys. Rev. B **84**, 054401 (2011).
[7] E. Blancá, J. Desimoni, N. Christensen, H. Emmerich, and S. Cottenier, The magnetization of γ'-Fe4N: theory vs. experiment, Phys. Status Solidi B **246**, 909 (2009).
[8] A. Gil Rebaza, J. Desimoni, and E. Peltzer y Blancá, Study on the oscillatory behaviour of the lattice parameter in ternary iron–nitrogen compounds, Physica (Amsterdam) **407B**, 3240 (2012).
[9] S. Kokado, N. Fujima, K. Harigaya, H. Shimizu, and A. Sakuma, Theoretical analysis of highly spin-polarized transport in the iron nitride Fe_4N, Phys. Rev. B **73**, 172410 (2006).
[10] K. Sunaga, M. Tsunoda, K. Komagaki, Y. Uehara, and M. Takahashi, Inverse tunnel magnetoresistance in magnetic tunnel junctions with an Fe_4N electrode, J. Appl. Phys. **102**, 013917 (2007).
[11] J. Jeong, Y. Ferrante, S. Faleev, M. Samant, C. Stuart, and S. Parkin, Termination layer compensated tunneling magnetoresistance in ferrimagnetic Heusler compounds with high perpendicular magnetic anisotropy, Nat. Commun. **7**, 10276 (2016).
[12] H. Yang, A. Vu, A. Hallal, N. Rougemaille, J. Coraux, G. Chen, A. Schmid, and M. Chshiev, Anatomy and giant enhancement of the perpendicular magnetic anisotropy of cobalt-graphene heterostructures, Nano Lett. **16**, 145 (2016).
[13] H. Hwang, Y. Iwasa, M. Kawasaki, B. Keimer, N. Nagaosa, and Y. Tokura, Emergent phenomena at oxide interfaces, Nat. Mater. **11**, 103 (2012).
[14] D. Kan, R. Aso, R. Sato, M. Haruta, H. Kurata, and Y. Shimakawa, Tuning magnetic anisotropy by interfacially engineering the oxygen coordination environment in a transition metal oxide, Nat. Mater. **15**, 432 (2016).
[15] Z. Liao, M. Huijben, Z. Zhong, N. Gauquelin, S. Macke, R. Green, S. Aert, J. Verbeeck, G. Tendeloo, K. Held, G. Sawatzky, G. Koster, and G. Rijnders, Controlled lateral anisotropy in correlated manganite heterostructures by interface-engineered oxygen octahedral coupling, Nat. Mater. **15**, 425 (2016).
[16] S. Mangin, D. Ravelosona, J. Katine, M. Carey, B. Terris, and E. Fullerton, Current-induced magnetization reversal in nanopillars with perpendicular anisotropy, Nat. Mater. **5**, 210 (2006).
[17] S. Brivio, D. Petti, R. Bertacco, and J. Cezar, Electric field control of magnetic anisotropies and magnetic coercivity in $Fe/BaTiO_3(001)$ heterostructures, Appl. Phys. Lett. **98**, 092505 (2011).
[18] G. Catalan and J. Scott, Physics and applications of bismuth ferrite, Adv. Mater. **21**, 2463 (2009).
[19] D. Ricinschi, K. Yun, and M. Okuyama, A mechanism for the 150 $\mu C/cm^{-2}$ polarization of $BiFeO_3$ films based on first-principles calculations and new structural data, J. Phys. Condens. Matter **18**, L97 (2006).
[20] H. Yamada, V. Garcia, S. Fusil, S. Boyn, M. Marinova, A. Gloter, S. Xavier, J. Grollier, E. Jacquet, C. Carrétéro, C. Deranlot, M. Bibes, and A. Barthélémy, Giant electroresistance of super-tetragonal $BiFeO_3$-based ferroelectric tunnel junctions, ACS Nano **7**, 5385 (2013).
[21] N. Feng, W. Mi, Y. Cheng, Z. Guo, U. Schwingenschlögl, and H. Bai, Magnetism by interfacial hybridization and p-type doping of MoS_2 in Fe_4N/MoS_2 superlattices: A first-principles study, ACS Appl. Mater. Interfaces **6**, 4587 (2014).
[22] A. Damodaran, C. Liang, Q. He, C. Peng, L. Chang, Y. Chu, and L. Martin, Nanoscale structure and mechanism for enhanced electromechanical response of highly strained $BiFeO_3$ thin films, Adv. Mater. **23**, 3170 (2011).
[23] P. Chen, N. Podraza, X. Xu, A. Melville, E. Vlahos, V. Gopalan, R. Ramesh, D. Schlom, and J. Musfeldt, Optical properties of quasi-tetragonal $BiFeO_3$ thin films, Appl. Phys. Lett. **96**, 131907 (2010).
[24] C. Pai, M. Mann, A. J. Tan, and G. Beach, Determination of spin torque efficiencies in heterostructures with perpendicular magnetic anisotropy, Phys. Rev. B **93**, 144409 (2016).
[25] P. Blöchl, Projector augmented-wave method, Phys. Rev. B **50**, 17953 (1994).
[26] J. Perdew, K. Burke, and M. Ernzerhof, Generalized Gradient Approximation Made Simple, Phys. Rev. Lett. **77**, 3865 (1996).
[27] N. Feng, W. Mi, X. Wang, Y. Cheng, and U. Schwingenschlogl, Superior properties of energetically stable $La_{2/3}Sr_{1/3}MnO_3$/tetragonal $BiFeO_3$ multiferroic superlattices, ACS Appl. Mater. Interfaces **7**, 10612 (2015).
[28] Y. Kim, A. Kumar, A. Hatt, A. Morozovska, A. Tselev, M. Biegalski, I. Ivanov, E. Eliseev, S. Pennycook, J. Rondinelli, S. Kalinin, and A. Borisevich, Interplay of octahedral tilts and polar order in $BiFeO_3$ films, Adv. Mater. **25**, 2497 (2013).
[29] J. Zhang, Q. He, M. Trassin, W. Luo, D. Yi, M. Rossell, P. Yu, L. You, C. Wang, C. Kuo, J. Heron, Z. Hu, R. Zeches, H. Lin, A. Tanaka, C. Chen, L. Tjeng, Y. Chu, and R. Ramesh, Microscopic Origin of the Giant Ferroelectric Polarization in Petragonal-like $BiFeO_3$, Phys. Rev. Lett. **107**, 147602 (2011).
[30] A. Narahara, K. Ito, T. Suemasu, Y. Takahashi, A. Ranajikanth, and K. Hono, Spin polarization of Fe_4N thin films determined by point-contact Andreev reflection, Appl. Phys. Lett. **94**, 202502 (2009).
[31] W. Mi, Z. Guo, X. Feng, and H. Bai, Reactively sputtered epitaxial γ'-Fe_4N films: Surface morphology, microstructure, magnetic, and electrical transport properties, Acta Mater. **61**, 6387 (2013).
[32] N. Caffrey, P. Ferriani, S. Marocchi, and S. Heinze, Atomic-scale inversion of spin polarization at an organic-antiferromagnetic interface, Phys. Rev. B **88**, 155403 (2013).

[33] T. Comyn, T. Stevenson, M. Al-Jawad, S. Turner, R. Smith, A. Bell, and R. Cywinski, High temperature neutron diffraction studies of $0.9BiFeO_3$-$0.1PbTiO_3$, J. Appl. Phys. **105**, 094108 (2009).

[34] S. Kanai, M. Tsujikawa, Y. Miura, M. Shirai, F. Matsukura, and H. Ohno, Magnetic anisotropy in Ta/CoFeB/MgO investigated by x-ray magnetic circular dichroism and first-principles calculation, Appl. Phys. Lett. **105**, 222409 (2014).

[35] Q. Zhang, S. Yang, W. Mi, Y. Cheng, and U. Schwingenschlögl, Large spin-valley polarization in monolayer $MoTe_2$ on top of EuO(111), Adv. Mater. **28**, 959 (2016).